

Quasi-2-day wave in low-latitude atmospheric winds as viewed from the ground and space during January-March, 2020

Maosheng He¹, Jorge L. Chau¹, Jeffrey M. Forbes², Xiaoli Zhang², Christoph
R. Englert³, Brian J. Harding⁴, Thomas J. Immel⁴, Lourivaldo M. Lima⁵, S.
Vijaya Bhaskar Rao⁶, M. Venkat Ratnam⁷, Guozhu Li^{8,9}, John M.
Harlander¹⁰, Kenneth D. Marr³, Jonathan J. Makela¹¹

¹Leibniz-Institute of Atmospheric Physics at the Rostock University, Kühlungsborn, Germany.

²Ann & H.J. Smead Department of Aerospace Engineering Sciences, University of Colorado, Boulder,
USA.

³U.S. Naval Research Laboratory, Washington, DC.

⁴Space Sciences Laboratory, University of California Berkeley, Berkeley, CA.

⁵Universidade Estadual da Paraíba, Brazil.

⁶Department of Physics, Sri Venkateswara University, Tirupati, India.

⁷National Atmospheric Research Laboratory, Tirupati, India.

⁸Beijing national observatory of space environment, Institute of Geology and Geophysics, Chinese
Academy of Sciences, Beijing, China.

⁹College of Earth and Planetary Sciences, University of Chinese Academy of Sciences, Beijing, China.

¹⁰Space Systems Research Corporation, Alexandria, VA.

¹¹Department of Electrical and Computer Engineering, University of Illinois at Urbana-Champaign,
Urbana, IL.

Key Points:

- Q2DW wind field at 80-200 km altitude is delineated from ground and space in the low-latitude region ($\pm 15^\circ$)
- Zonal wavenumber components $s = +2$ and $s = +3$ are the dominant ones in our observations, and their wave periods evolve differently with time.
- The Q2DW+3 exhibits an excellent quantitative agreement between two datasets at 95–100 km, serving as a validation of the ICON-MIGHTI winds.

Corresponding author: Jorge L. Chau, chau@iap-kborn.de

Abstract

Horizontal winds from four low-latitude ($\pm 15^\circ$) specular meteor radars (SMRs) and the MIGHTI instrument on the ICON satellite, are combined to investigate quasi-2-day waves (Q2DWs) in early 2020. SMRs cover 80-100 km altitude whereas MIGHTI covers 95-300 km. Q2DWs are the largest dynamical feature of the summertime middle atmosphere. At the overlapping altitudes, comparisons between the derived Q2DWs exhibit excellent agreement. The SMR sensor array analyses show that the dominant zonal wavenumbers are $s = +2$ and $+3$, and help resolve ambiguities in MIGHTI results. We present the first Q2DW depiction for $s = +3$ up to 200 km and for $s = +2$ above 95 km, and show that their amplitudes are almost invariant between 80 and 100 km. Above 106 km, Q2DW amplitudes and phases present structures that might result from the superposition of Q2DWs and their aliased secondary waves.

Plain Language Summary

In the mesosphere and lower-thermosphere, quasi-2-day waves are spectacular planetary-scale oscillations. Almost all relevant observational studies are based on ground-based single-station or single-satellite methods and therefore cannot determine the zonal wavenumber unambiguously. In the current work, we employ a series of multi-station methods on winds measured by four longitudinally separated low-latitude ground-based radars. These methods help us to determine two dominant zonal wavenumbers at 80–100 km altitude. These results are used to complement satellite measurements. The agreement between datasets is extraordinary, allowing us to extend the characteristics of the waves to higher altitudes using satellite measurements.

1 Introduction

Quasi-two-day waves (Q2DWs) in the mesosphere have been the subject of numerous observational and theoretical investigations (e.g., Pancheva et al., 2018, and references therein) since their first discovery in specular meteor radar (SMR) winds (Müller, 1972). Q2DWs are generally thought to be the atmospheric manifestation of the gravest westward-propagating Rossby-gravity normal mode with zonal wavenumber $s = 3$ (Salby & Roper, 1980; Salby, 1981), amplified or perhaps even initiated by the mesospheric eastward jet instability (Randel, 1994; Plumb, 1983; Pfister, 1985), which admits zonal wavenumbers of $s = 2$ through 4. Q2DWs with $s = 2, 3,$ and 4 are common features of space-based observational studies (e.g., Lieberman, 1999; Tunbridge et al., 2011; Gu et al., 2013; Huang et al., 2013).

Being the largest dynamical features of the summertime middle atmosphere, Q2DWs play a significant role in atmosphere-ionosphere coupling. Although earlier works have suggested that Q2DWs could drive F-region ionospheric variability (Ito et al., 1986; Chen, 1992; Pancheva, 1988; Pancheva & Lysenko, 1988), it was not until the last decade that a general circulation model (GCM) including ionospheric electrodynamics demonstrated that the Q2DWs could penetrate above 100 km to produce dynamo electric fields that drive Q2DW ionospheric variability in the F-region (Yue, Wang, et al., 2012). However, it is also known that such penetration is highly sensitive to the zonal-mean wind distribution above 100 km, which is poorly specified (Yue, Liu, & Chang, 2012). In addition, there are remaining questions concerning other ways in which Q2DWs transmit their influence to the ionosphere, including the modulation of tides (Yue et al., 2016) and gravity waves (Meyer, 1999). Other relevant aspects of the problem include the latitude and longitude structure of Q2DWs at any given time. Therefore, further study of the spatial-temporal evolution of Q2DWs and their interactions with other waves appears warranted before a complete understanding of atmosphere-ionosphere coupling is attained.

The pros and cons of ground- and space-based measurements of Q2DWs in the mesosphere and lower thermosphere (MLT) are well-known. Single-station ground-based measurements provide excellent temporal resolution but no information on their horizontal wavenumber (e.g., Harris & Vincent, 1993). On the other hand, satellite measurements provide a more global view in terms of spatial coverage, but suffer from crude temporal resolution and, most significantly, aliasing (Tunbridge et al., 2011; Forbes & Moud-

den, 2012; Nguyen et al., 2016). When viewed from a quasi-Sun-synchronous perspective in space, a wave at frequency f with zonal wavenumber s is Doppler-shifted such that its longitude structure appears at its “space-based zonal wavenumber” $k_s = |s - \frac{f}{1\text{cpd}}|$, where cpd is cycles per day (e.g., Forbes & Moudden, 2012).

Accordingly, the Q2DW+3 (hereafter, Q2DW p denotes a Q2DW with wavenumber $s = p$) appears at $k_s = 2.5$, and so do secondary waves (SWs) of nonlinear interactions between Q2DW+3 and all migrating tides (Tunbridge et al., 2011; Forbes & Moudden, 2012; Nguyen et al., 2016). These SWs are at frequencies near 0.5, 1.5, 2.5, 3.5, ..., cpd, namely, at periods near 2 day, 16 h, 9.6 h, 6.9 h,... (e.g., He et al., 2021). In other words, these waves will alias into each other when observed from quasi-Sun-synchronous single-spacecraft missions. Among these waves is the Q2DW-2, the near-2-day SW from a Q2DW+3 interaction with the migrating diurnal tide. Similarly, Q2DW+2 and Q2DW+4 can alias with Q2DW-1 and Q2DW-3 at $k_s = 2.5$ and 3.5, respectively. Both Q2DW-2 and Q2DW-3 can arise from jet instabilities at middle to high latitudes during local winter (Pancheva et al., 2016), and all three eastward-propagating Q2DWs can coexist at low latitudes in the form of ultra-fast Kelvin waves (UFKW)(e.g., Forbes, He, et al., 2020; Pancheva et al., 2016).

Despite the importance of dynamo-region winds to Q2DW-ionosphere coupling, wind observations are extremely rare above about 105 km. One exception appears to be Ward et al. (1996) who reported Q2DW+3 winds between 90 and 150 km from Wind Imaging Interferometer (WINDII) daytime measurements on the Upper Atmosphere Research Satellite (UARS) during January 1993. Nighttime satellite measurements are unavailable above 105–110 km due to lack of airglow. This exacerbates sampling issues associated with space-based observations. But combining ground and space partially alleviates this ambiguity, as shown in this study.

As suggested by Harris and Vincent (1993), combining more than one ground-based station could enable a determination of Q2DWs wavenumbers. In the present work, we combine horizontal winds from multiple SMRs (MSMR) located at four different longitudes at low latitudes, and from MIGHTI (Michelson Interferometer for Global High-resolution Thermospheric Imaging) on NASA’s ICON (Ionospheric CONnection explorer) satellite (Immel et al., 2018). This combination allows us to obtain a comprehensive view of the Q2DWs that occurred during January–March 2020. Combining the MSMR and

115 MIGHTI analyses, we are able to characterize clearly the dominant Q2DWs in time, al-
 116 titude, frequency, wavenumber, and latitude.

117 2 Data analysis

118 The current work investigates Q2DWs using MLT zonal (u) and meridional (v) winds
 119 collected on the ground and from space. Ground-based winds were obtained between 80
 120 and 100 km every hour at four SMRs: Peru (77°W , 12°S), and Cariri (36.5°W , 7.4°S),
 121 Tirupati (79.4°E , 13.6°N) and Ledong (109.0°E , 18.4°N). Characteristics and some re-
 122 sults of each of these SMRs can be found in Chau et al. (2021), Lima et al. (2012), S. V. B. Rao
 123 et al. (2014), and Wang et al. (2019), respectively. The space-based winds are collected
 124 by the MIGHTI instrument on ICON (Englert et al., 2017). From a theoretical study,
 125 MIGHTI's wind accuracy is better than 5.8 ms^{-1} 80% of the time. The exceptions oc-
 126 cur near the day/night boundaries and occasionally near the equatorial ionization anomaly
 127 (in the F-region), due to variations of wind and emission rate along the line-of-sight (Harding
 128 et al., 2017). Recently, MIGHTI winds in the F-region (red line) and E-region (green line)
 129 have been validated against Fabry-Perot interferometers and SMRs, respectively (Makela
 130 et al., 2021; Harding et al., 2021). At low latitudes, Q2DWs maximize annually during
 131 January and March (e.g., Harris & Vincent, 1993; N. V. Rao et al., 2017), thus, our study
 132 is focused on the January–March 2020 period.

133 2.1 Multi-station specular meteor radar analyses

134 At a given frequency f , longitude λ , and time t , the superposition of zonal trav-
 135 eling waves, indexed as $l = 1, 2, \dots, L$, with zonal wavenumbers s_l , can be denoted as,

$$\sum_{l=1,2,\dots,L} \tilde{\Psi}(\lambda, t|f, s_l) = e^{i2\pi ft} \tilde{a}_\lambda \quad (1)$$

136 where $\tilde{a}_\lambda = \sum \tilde{A}(\lambda|s_l)$ and $\tilde{A}(\lambda|s_l) = \tilde{A}_l e^{is\lambda}$ is the longitude-dependent complex am-
 137 plitude. We estimate \tilde{a}_λ as a function of f , t , and altitude h , through Lomb-Scargle spec-
 138 tral analyses within a 23-day wide sliding window for each of the wind components of
 139 each SMR. The resultant $\tilde{a}_\lambda(t, f, h)$ enable estimation of s and \tilde{A}_l using a variety of sen-
 140 sor array analyses.

141 Assuming a single dominant wave, i.e., $L = 1$, one can apply the phase difference
 142 technique to a pair of SMRs (e.g., He et al., 2018). The single-wave assumption is of-

143 ten facilitated through high-frequency-resolved wavelet or Lomb-Scargle analyses by sep-
 144 arating waves in the frequency domain (e.g., He et al., 2018). The current work applies
 145 this technique to Tirupati-Ledong and Peru-Cariri pairs, separately. These pairs have
 146 been selected given their similar latitudes and relative close longitudinal proximity.

147 The same wind data have also been analyzed, assuming a dominant wave (i.e., $L =$
 148 1) weakly dependent in latitude. In this case, a least-square estimation (LSE) method
 149 similar to Equation A3 in He et al. (2020) has been applied to the altitude-averaged Lomb-
 150 Scargle estimations $\langle \tilde{a}_\lambda(t, f, h) \rangle$ from all four radars. This analysis allows determining
 151 the dominant wavenumbers for a given period and time.

152 As we will see later in Section 3, the techniques implemented above reveal that the
 153 Q2DWs are dominated mainly by two wavenumbers. While the above techniques use the
 154 single-wave assumption, these two dominant waves might superpose on each other. To
 155 decompose the potential superposition and estimate the wave amplitudes, we implement
 156 an LSE to Equation (1) after relaxing the single-wave assumption to a two-wave assump-
 157 tion, i.e., $L = 2$. A similar procedure was applied by He and Chau (2019) but for near-
 158 12-h waves. In the results presented below, the amplitudes are set to zeros either when
 159 $\langle \tilde{a}_\lambda(t, f, h) \rangle$ are below the significance level $\alpha = 0.01$ at more than two stations or when
 160 the coefficient of determination of the LSE is below $r^2 = 0.7$. The significance level is
 161 estimated through a Monte Carlo method.

162 2.2 ICON-MIGHTI winds

163 As a slowly precessing low-earth-orbit satellite, ICON orbits at 590–607 km alti-
 164 tude about 15 times per day. ICON crosses a given latitude once in the ascending or de-
 165 scending leg which crosses all local solar times once every 46 days, namely, one orbital
 166 precession period. Constrained by the 27° orbital inclination and MIGHTI’s viewing ge-
 167 ometry off the north side of the spacecraft, the winds are derived between 12°S and 42°N
 168 latitude. The ascending-descending differences in the local time are latitude-dependent,
 169 which increases from near zero at 12°S to almost 12 h near 18°N and then decreases to
 170 less than 2 h at 42°N . MIGHTI winds are derived from the Doppler shift of airglow emis-
 171 sions along with two perpendicular tangent-point line-of-sight vector measurements on
 172 the limb. Due to the day-night difference of the airglow’s vertical distribution, the al-
 173 titude coverage of the observations is different between day and night. While the night-

174 time wind is derived from about 94–106 km, the daytime wind is available at least up
 175 to 300 km. In this work, we use the green-line winds, which cover up to 200 km (e.g.,
 176 Harding et al., 2021).

177 At 96–106 km altitude, we estimate Q2DW amplitudes as a function of time, fre-
 178 quency, latitude and altitude, by fitting data sampled within a 23-day sliding window,
 179 irrespective of the local time, to a single wave model $\tilde{A}_0(s)e^{i(2\pi ft+s\lambda)}$, for $s = 2$ and
 180 3, respectively. Above 106 km and for the amplitude fitting, we sample the only-daytime-
 181 available data within time intervals when strong Q2DWs are detected below 106 km, e.g.,
 182 DOY (day of the year) 15–23 and DOY 39–46. As an example of the data distribution
 183 within these two intervals, Figure S1 in the supplemental information presents the sam-
 184 plings as a function of time and subdivided longitude (cf, Moudden & Forbes, 2014) at
 185 a given latitude and altitude.

186 **3 Results**

187 Under the single-wave assumption, dominant wavenumbers were obtained by (a)
 188 using the phase difference technique on SMR pairs, and (b) using LSE on all four SMRs
 189 but assuming a weak latitudinal dependence. We found that in both cases the dominant
 190 Q2DW wavenumbers were $s = 3$ and $s = 2$, i.e., Q2DW+3, and Q2DW+2, respec-
 191 tively. Furthermore, we find that the meridional component is much stronger than the
 192 zonal component for both dominant wavenumbers. The results of these two analyses are
 193 presented in the supplemental material Figures S2 and S3, respectively.

194 Based on these supporting results, we present the results of relaxing the assump-
 195 tion of one dominant wavenumber for a given time, frequency and altitude, to allow two,
 196 i.e., $L = 2$. Figure 1 shows the meridional amplitudes as a function of time and period
 197 resulting from fitting for $s = 2$ (left) and $s = 3$ (right) at four altitude ranges, i.e., 80-
 198 85 km, 85-90 km, 90-95 km, and 95-100 km.

199 As displayed in Figure 1a(1b), the Q2DW+2(Q2DW+3) amplitude at 95–100 km
 200 altitude maximizes within DOY 40–75(10–40) at period 44–48(48–53) h above 15 ms^{-1} (30 ms^{-1}).
 201 The period and amplitude variations of Q2DW+2 and Q2DW+3 at 95–100 km altitude
 202 are similar to those at the other three altitudes.

203 MIGHTI winds complement the MSMR results by extending the Q2DW amplitudes
 204 to broader latitude and altitude ranges. In the time-latitude structures of the MIGHTI

205 Q2DWs at 98 km, as shown in Figure 2, the meridional wind (v) amplitudes of both Q2DWs
 206 are significantly stronger than the zonal wind (u) amplitudes, consistent with MSMR
 207 results in Figure S2. In v , both Q2DWs attain values of order 20–30 ms^{-1} within $\pm 12^\circ$
 208 latitude and maximize around the equator. The u amplitudes attain values above 10 ms^{-1}
 209 which is confined to latitudes poleward of 10°N .

210 In Figure 3 we present a qualitative and quantitative comparison of the estimated
 211 Q2DW amplitudes obtained with MSMR and MIGHTI. In Figures 3a–3d, the time-frequency
 212 spectra of the MSMR Q2DW amplitudes at 95–100 km are in a good qualitative agree-
 213 ment with MIGHTI estimates at 98 km. For a quantitative comparison, we sample ev-
 214 ery pixel in the MIGHTI spectra of Q2DW+2 and Q2DW+3 and scatter them against
 215 the corresponding MSMR amplitudes in Figures 3e and 3f, respectively. Overall, the MIGHTI
 216 Q2DW+2 is stronger than the MSMR amplitudes. The former attains 20–25 ms^{-1} whereas
 217 the latter is below 15 ms^{-1} . In the case of Q2DW+3, MIGHTI results exhibit excellent
 218 quantitative agreement with the MSMR results, both of which attain 30 ms^{-1} .

219 The fitted amplitudes and phases for MIGHTI results above 96 km are shown in
 220 Figure 4 as a function of height at 0° and 15°N latitude. The profiles centered on -5° ,
 221 $+5^\circ$ and $+25^\circ$ are not sufficiently different from neighboring profiles and therefore not
 222 shown here. Within DOY 15–23, the amplitudes maximize generally below 140 km where
 223 the profiles often possess two peaks. Also, the v maximum is about a factor of two smaller
 224 ($\lesssim 10 \text{ ms}^{-1}$) for Q2DW+2 as compared with Q2DW+3 ($\sim 20 \text{ ms}^{-1}$), whereas the u max-
 225 imum for Q2DW+2 (12–14 ms^{-1}) is slightly larger than that for Q2DW+3. In addition,
 226 half the amplitude profiles show increases with altitude above a minimum near 140–150 km
 227 altitude, suggesting a source at higher altitudes. The profiles within DOY 41–49 share
 228 many of the same characteristics.

229 4 Discussions

230 In the low-latitude middle atmosphere, Q2DWs maximize annually during late Jan-
 231 uary and early February (Palo & Avery, 1996; Harris & Vincent, 1993). Harris and Vin-
 232 cent (1993) noted that the Q2DW-like oscillation in January–February 1991 occurs pre-
 233 dominantly at a period 48–50 h, associated with a weaker one at 44 h. According to these
 234 periods the authors suggested that the oscillations are manifestations of Rossby-gravity
 235 modes Q2DW+3 and Q2DW+2, but could not determine s since they used single-station

236 observations. Our multi-station analyses reveal that during January–February 2020 the
 237 most dominant Q2DWs are Q2DW+3 at 48–53 h and Q2DW+2 at 44–48 h. In addition,
 238 we find that: (a) the maximum Q2DW+3 amplitude is much stronger than the Q2DW+2
 239 maximum, by a factor of about two, and (b) the Q2DW+3 are almost invariant within
 240 80–100 km altitude, although slightly weaker at 80–85 km than at 85–100 km. Our anal-
 241 yses are the first to directly support the wavenumber suggestions of Harris and Vincent
 242 (1993).

243 Note that our MSMR amplitudes are fitted according to the model of two waves
 244 with preassigned s which have to be determined prior to the fitting. Therefore, when the
 245 spectrum in the time-frequency depiction is dominated by a third s , the estimation can-
 246 not be properly fitted. For example, in Figure S3 besides $s = +3$ and $+2$, the $s = +1$
 247 and $+4$ dominate also few pixels within DOY 1–60. At these pixels, the amplitudes are
 248 not fitted for Q2DW+1 and Q2DW+4 due to constraints of the two-wave model ($r^2 <$
 249 0.7). Besides, these four dominant Q2DWs might interact nonlinearly with diurnal mi-
 250 grating tides, generating SWs of Q2DW-3, Q2DW-2, Q2DW-1, and , Q2DW0. Additional
 251 low-latitude SMRs are desirable to resolve the above-mentioned Q2DWs.

252 In terms of the temporal evolution of Q2DW+3 amplitude and periods, MSMR re-
 253 sults at 95–100 km are in excellent qualitative agreement with the MIGHTI results. The
 254 agreement reveals that locally Q2DW+3 is dominantly stronger than its potential aliased
 255 waves, e.g., Q2DW-2, near-16-h and -9.6-h SWs, and near-2-day UFKW at $s = -2$, as
 256 explained in the introduction. Therefore MSMR help to resolve this type of ambiguity
 257 in MIGHTI Q2DW results. However, Q2DW+2 are stronger in the MIGHTI winds than
 258 in MSMR winds. The discrepancy is possibly attributable to a superposition in the MIGHTI
 259 amplitude between Q2DW+2 and its potential aliased waves, e.g., Q2DW-1.

260 At altitudes not covered by MSMRs, e.g., above 106 km, the aliased and the su-
 261 perposition might also exist. The superposition could produce the vertical double-peak
 262 feature below 140 km altitude observed in Figure 4, associated in some cases with dis-
 263 continuities, which would be unexpected for a vertically-propagating monochromatic wave.
 264 The phases often show downward(upward) phase progressions with altitude, indicative
 265 of upward(downward) energy propagation. MLT GCM simulations produced near-48-
 266 h, -16-h, -9.6-h SWs arising from interactions of Q2DW+3 with diurnal and semidiur-
 267 nal migrating tides (Palo et al., 1999; Nguyen et al., 2016; Gu et al., 2018). These SWs

268 appear in the simulations as independent, global-scale vertically-propagating oscillations
269 that extend to at least 50°N in January. Moreover, the simulations demonstrate that these
270 SWs are capable of propagating into the 100–140 km region, and in some cases, above
271 160 km. It is, therefore, reasonable to assume that during Q2DW events, measurable SWs
272 can simultaneously occur over broad latitude-altitude regimes, and that more appropri-
273 ate designations in the context of space-based observations are “apparent” Q2DW+2,
274 Q2DW+3, and Q2DW+4.

275 No studies to date have considered the possibility of SW generation in the lower
276 and middle thermosphere ($\sim 100\text{--}250$ km) where the migrating tidal winds exist due to
277 thermal forcing by extreme ultraviolet solar radiation, and where the vertically-propagating
278 semidiurnal migrating tide maintains large amplitudes (Figure 6 in Forbes, Zhang, & Maute,
279 2020). Palo et al. (1999) furthermore invoked the Teitelbaum and Vial (1991) formula-
280 tion of wave-wave interactions to demonstrate that a myriad of wave products can origi-
281 nate from multi-step SW-tide interactions, including the secondary Q2DWs as products,
282 which complicates the aliasing situation. This secondary Q2DW production parallels the
283 secondary production of the thermospheric Q6DW (demonstrated quantitatively in Forbes,
284 Zhang, & Maute, 2020). Our interpretation that these processes are likely active in defin-
285 ing the vertical amplitude and phase structures of Q2DW+3 and Q2DW+2 in Figure
286 4 warrants further theoretical and modeling attention.

287 A similar double-peak feature was also observed in the southern hemisphere Q2DW+3
288 in WINDII v profiles up to 150 km during January 19–31, 1993 (Ward et al., 1996). Dur-
289 ing this event, Q2DW+3 amplitudes and phases were estimated between 96–102 km and
290 70°S – 40°N using WINDII, between 70–110 km and 60°S – 20°N using the High Resolu-
291 tion Doppler Imager (HRDI) on UARS, and between 94–136 km altitude using winds
292 collected by the Arecibo incoherent scatter radar (18°N) (Wu et al., 1993). Furthermore,
293 the UARS analyses assumed $T = 48$ h and $s = 3$.

294 In terms of Q2DW penetration into the winter hemisphere, the UARS results at
295 95–100 km are consistent with our Q2DW+3 results in that they (a) reflect an equato-
296 rial maximum in v with a monotonic decrease to less than half the maximum value by
297 30°N , and (b) a minimum in u at the equator and maximum as far north as $30\text{--}40^\circ$
298 latitude. However, both the u and v maxima are about a factor of 2 greater during 1993
299 than during 2020.

300 From a more global perspective, Ward et al. (1996) noted in their Figure 3 the sim-
 301 ilarity of the meridional 3-peaked(2-peaked) structure of $u(v)$ between 70°S – 40°N with
 302 those in the Q2DW+3 simulations of Hagan et al. (1993). Similar features are also seen
 303 in Palo et al. (1999) simulations, but the GCM $u(v)$ structures in Yue, Wang, et al. (2012)
 304 are more 2-peaked(1-peaked). All of these results maintain an equatorial minimum in
 305 u and a monotonic decrease in v poleward of the equator into the Northern Hemisphere.
 306 The tendency for an equatorial maximum in v , and maxima in u poleward of the equa-
 307 tor is consistent with the attribution of Q2DW+3 as a Rossby-gravity wave. Therefore,
 308 the latitude structures of v and u for Q2DW+3 depicted in Figures 2a and 2c at 98 km
 309 are broadly consistent with prior observations, theory, and modeling.

310 Another unique aspect of the current work is the delineation of both Q2DW+3 and
 311 Q2DW+2 vertical structures up to 200 km altitude during a period of deep solar min-
 312 imum, when vertically-propagating waves should penetrate efficiently in the thermosphere
 313 (Oberheide et al., 2009; Häusler et al., 2013). Of particular relevance is the degree to which
 314 the Q2DW wind field penetrates to altitudes in the vicinity of the peak Hall (~ 106 km)
 315 and Pedersen (~ 125 km) conductivities, where electric fields can be generated and sub-
 316 sequently map into the F-region. This vertical penetration is in fact reflected in Figure
 317 4, but it remains to be determined to what extent the amplitudes and vertical phase struc-
 318 tures yield sufficiently large field-aligned-integrated conductivity-weighted winds to drive
 319 F-region ionospheric variability of any significance.

320 5 Summary and conclusions

321 In this work, we combine MLT winds observed by four longitudinally separated low-
 322 latitude SMRs and by MIGHTI on the ICON satellite to investigate Q2DWs during January–
 323 March 2020. Based on different but complementary sensor array analyses, we identify
 324 that Q2DWs are dominated by Q2DW+3 and Q2DW+2, at periods $T = 48$ – 53 h and
 325 44 – 48 h, respectively. These are the first observations of such waves and support the sug-
 326 gested Q2DW wavenumbers of Harris and Vincent (1993) based on single-station obser-
 327 vations.

328 Our MSMR Q2DW amplitudes are almost altitude-independent within 80–100 km.
 329 Their 95–100 km time-frequency structures compared well with the amplitudes estimated
 330 from MIGHTI winds. In the comparison, Q2DW+3 exhibits an excellent quantitative

331 agreement whereas the Q2DW+2 exhibits only a reasonable qualitative agreement with
332 stronger amplitudes in MIGHTI than in MSMR results. Based on this agreement, we
333 are able to resolve the period and wavenumber ambiguity in MIGHTI estimates. We at-
334 tribute the discrepancy to the existence of aliased waves.

335 The MIGHTI measurements are further used to assess the degree of latitudinal and
336 vertical penetration of the Q2DWs, up to 42°N and 200 km. At 98 km and for both Q2DW+2
337 and Q2DW+3, the amplitudes in v are stronger than in u . For Q2DW+3, these features
338 are largely consistent with prior observations, theory and modeling, whereas for Q2DW+2
339 the height-latitude structures have not appeared in prior observational or modeling stud-
340 ies. Above 106 km, the amplitudes become vertically structured. These vertical struc-
341 tures are attributable to the superposition between Q2DWs and their aliased waves.

342 Acknowledgments

343 This work was supported by the Deutsche Forschungsgemeinschaft (DFG, German Re-
344 search Foundation) under SPP 1788 (DynamicEarth)-CH 1482/1-2 (DYNAMITE). C.
345 Englert, J. Forbes, B. Harding, T. Immel, J. Makela, J. Harlander, K. Marr, and X. Zhang
346 gratefully acknowledge support for this project by the ICON mission, which is supported
347 by NASA's Explorers Program through contracts NNG12FA45C and NNG12FA42I. G.
348 Li acknowledges the support of NSFC (42020104002, 41727803).

349 Open Research Data Statement

350 The hourly wind data from Ledong is provided by the Data Center for Geophysics,
351 National Earth System Science Data Sharing Infrastructure at BNOSE, IGGCAS ([http://](http://wdc.geophys.ac.cn/)
352 wdc.geophys.ac.cn/). The post-processed MSMR data used in the current paper are
353 available at DOI 10.22000/421 ([https://www.radar-service.eu/radar/en/dataset/](https://www.radar-service.eu/radar/en/dataset/sHWduLXVNoaZNhUQ?token=ZVxakQZEdrDaNMpWpgtF)
354 [sHWduLXVNoaZNhUQ?token=ZVxakQZEdrDaNMpWpgtF](https://www.radar-service.eu/radar/en/dataset/sHWduLXVNoaZNhUQ?token=ZVxakQZEdrDaNMpWpgtF)). The ICON-MIGHTI winds are pub-
355 licly available at the ICON data center (<https://ICON/MIGHTI.ssl.berkeley.edu/Data>).

356 References

357 Chau, J. L., Urco, J. M., Vierinen, J., Harding, B. J., Clahsen, M., Pfeffer, N., . . .
358 Erickson, P. J. (2021). Multistatic Specular Meteor Radar Network in Peru:
359 System Description and Initial Results. *Earth Sp. Sci.*, 8(1), e2020EA001293.
360 doi: 10.1029/2020EA001293

- 361 Chen, P.-R. (1992). Two-day oscillation of the equatorial ionization anomaly. *J.*
 362 *Geophys. Res.*, *97*(A5), 6343. doi: 10.1029/91ja02445
- 363 Englert, C. R., Harlander, J. M., Brown, C. M., Marr, K. D., Miller, I. J., Stump,
 364 J. E., ... Immel, T. J. (2017). Michelson Interferometer for Global High-
 365 Resolution Thermospheric Imaging (MIGHTI): Instrument Design and Cal-
 366 ibration. *Space Sci. Rev.*, *212*(1-2), 553–584. Retrieved from [https://](https://doi.org/10.1007/s11214-017-0358-4)
 367 doi.org/10.1007/s11214-017-0358-4 doi: 10.1007/s11214-017-0358-4
- 368 Forbes, J. M., He, M., Maute, A., & Zhang, X. (2020). Ultrafast Kelvin Wave
 369 Variations in the Surface Magnetic Field. *J. Geophys. Res. Sp. Phys.*, *125*(9),
 370 e2020JA028488. Retrieved from <https://doi.org/10.1029/2020JA028488>
 371 doi: 10.1029/2020JA028488
- 372 Forbes, J. M., & Moulden, Y. (2012). Quasi-two-day wave-tide interactions as re-
 373 vealed in satellite observations. *J. Geophys. Res. Atmos.*, *117*(12). Retrieved
 374 from <https://doi.org/10.1029/2011JD017114> doi: 10.1029/2011JD017114
- 375 Forbes, J. M., Zhang, X., & Maute, A. (2020). Planetary Wave (PW) Generation in
 376 the Thermosphere Driven by the PW-Modulated Tidal Spectrum. *J. Geophys.*
 377 *Res. Sp. Phys.*, *125*(5), 1–19. doi: 10.1029/2019JA027704
- 378 Gu, S. Y., Li, T., Dou, X., Wu, Q., Mlynczak, M. G., & Russell, J. M. (2013). Ob-
 379 servations of Quasi-Two-Day wave by TIMED/SABER and TIMED/TIDI. *J.*
 380 *Geophys. Res. Atmos.*, *118*(4), 1624–1639. doi: 10.1002/jgrd.50191
- 381 Gu, S. Y., Liu, H. L., Dou, X., & Jia, M. (2018). Ionospheric Variability Due to
 382 Tides and Quasi-Two Day Wave Interactions. *J. Geophys. Res. Sp. Phys.*,
 383 *123*(2), 1554–1565. doi: 10.1002/2017JA025105
- 384 Hagan, M. E., Forbes, J. M., & Vial, F. (1993). Numerical investigation of the
 385 propagation of the quasi-two-day wave into the lower thermosphere. *J. Geo-*
 386 *phys. Res.*, *98*(D12), 23193. doi: 10.1029/93jd02779
- 387 Harding, B. J., Chau, J. L., He, M., Englert, C. R., Harlander, J. M., Marr, K. D.,
 388 ... Immel, T. J. (2021). Validation of ICON-MIGHTI thermospheric wind
 389 observations: 2. Green-line comparisons to specular meteor radars. *J. Geophys.*
 390 *Res. Sp. Phys.*, e2020JA028947. doi: <https://doi.org/10.1029/2020JA028947>
- 391 Harding, B. J., Makela, J. J., Englert, C. R., Marr, K. D., Harlander, J. M., Eng-
 392 land, S. L., & Immel, T. J. (2017). The MIGHTI Wind Retrieval Algo-
 393 rithm: Description and Verification. *Space Sci. Rev.*, *212*(1-2), 585–600.

- 394 Retrieved from <https://doi.org/10.1007/s11214-017-0359-3> doi:
395 10.1007/s11214-017-0359-3
- 396 Harris, T. J., & Vincent, R. A. (1993). The quasi-two-day wave observed in the
397 equatorial middle atmosphere. *J. Geophys. Res.*, *98*(D6), 10481. doi: 10.1029/
398 93jd00380
- 399 Häusler, K., Oberheide, J., Lühr, H., & Koppmann, R. (2013). The geospace re-
400 sponse to nonmigrating tides. In *Clim. weather sun-earth syst.* (pp. 481–506).
401 Springer.
- 402 He, M., & Chau, J. L. (2019). Mesospheric semidiurnal tides and near-12 h
403 waves through jointly analyzing observations of five specular meteor radars
404 from three longitudinal sectors at boreal midlatitudes. *Atmos. Chem.*
405 *Phys.*, *19*(9), 5993–6006. Retrieved from [https://doi.org/10.5194/
406 acp-19-5993-2019](https://doi.org/10.5194/acp-19-5993-2019) doi: 10.5194/acp-19-5993-2019
- 407 He, M., Chau, J. L., Stober, G., Li, G., Ning, B., & Hoffmann, P. (2018). Re-
408 lations Between Semidiurnal Tidal Variants Through Diagnosing the Zonal
409 Wavenumber Using a Phase Differencing Technique Based on Two Ground-
410 Based Detectors. *J. Geophys. Res. Atmos.*, *123*(8), 4015–4026. Retrieved from
411 <https://doi.org/10.1002/2018JD028400> doi: 10.1002/2018JD028400
- 412 He, M., Forbes, J. M., Chau, J. L., Li, G., Wan, W., & Korotyshkin, D. V. (2020).
413 High-Order Solar Migrating Tides Quench at SSW Onsets. *Geophys. Res.*
414 *Lett.*, *47*(6), 1–8. Retrieved from <https://doi.org/10.1029/2019GL086778>
415 doi: 10.1029/2019GL086778
- 416 He, M., Forbes, J. M., Li, G., Jacobi, C., & Hoffmann, P. (2021). Mesospheric
417 Q2DW interactions with four migrating tides at 53N latitude: zonal wavenum-
418 ber identification through dual-station approaches. *Geophys. Res. Lett.*, *48*,
419 e2020GL092237. Retrieved from <https://doi.org/10.1029/2020GL092237>
420 doi: 10.1029/2020GL092237
- 421 Huang, Y. Y., Zhang, S. D., Yi, F., Huang, C. M., Huang, K. M., Gan, Q., & Gong,
422 Y. (2013). Global climatological variability of quasi-two-day waves revealed
423 by TIMED/SABER observations. *Ann. Geophys.*, *31*(6), 1061–1075. Re-
424 trieved from <https://angeo.copernicus.org/articles/31/1061/2013/> doi:
425 10.5194/angeo-31-1061-2013
- 426 Immel, T. J., England, S. L., Mende, S. B., Heelis, R. A., Englert, C. R., Edelstein,

- 427 J., ... Sirk, M. M. (2018). The Ionospheric Connection Explorer Mission:
 428 Mission Goals and Design. *Space Sci. Rev.*, *214*(1). Retrieved from [https://](https://doi.org/10.1007/s11214-017-0449-2)
 429 doi.org/10.1007/s11214-017-0449-2 doi: 10.1007/s11214-017-0449-2
- 430 Ito, R., Kato, S., & Tsuda, T. (1986). Consideration of an ionospheric wind dynamo
 431 driven by a planetary wave with a two-day period. *J. Atmos. Terr. Phys.*,
 432 *48*(1), 1–13. doi: 10.1016/0021-9169(86)90108-X
- 433 Lieberman, R. S. (1999). Eliassen-Palm Fluxes of the 2-Day Wave. *J. Atmos. Sci.*,
 434 *56*(16), 2846–2861. doi: 10.1175/1520-0469(1999)056<2846:EPFOTD>2.0.CO;
 435 2
- 436 Lima, L. M., Alves, E. O., Batista, P. P., Clemesha, B. R., Medeiros, A. F., &
 437 Burity, R. A. (2012). Sudden stratospheric warming effects on the meso-
 438 spheric tides and 2-day wave dynamics at 7°S. *J. Atmos. Solar-Terrestrial*
 439 *Phys.*, *78-79*, 99–107. Retrieved from [http://dx.doi.org/10.1016/](http://dx.doi.org/10.1016/j.jastp.2011.02.013)
 440 [j.jastp.2011.02.013](http://dx.doi.org/10.1016/j.jastp.2011.02.013) doi: 10.1016/j.jastp.2011.02.013
- 441 Makela, J. J., Baughman, M., Navarro, L. A., Harding, B. J., Englert, C. R.,
 442 Harlander, J. M., ... Immel, T. J. (2021). Validation of ICON-MIGHTI
 443 Thermospheric Wind Observations: 1. Nighttime Red-Line Ground-Based
 444 Fabry-Perot Interferometers. *J. Geophys. Res. Sp. Phys.*, *126*(2), 1–13. doi:
 445 10.1029/2020ja028726
- 446 Meyer, C. K. (1999). Gravity wave interactions with mesospheric planetary
 447 waves: A mechanism for penetration into the thermosphere-ionosphere sys-
 448 tem. *J. Geophys. Res. Sp. Phys.*, *104*(A12), 28181–28196. Retrieved from
 449 <https://doi.org/10.1029/1999ja900346> doi: 10.1029/1999ja900346
- 450 Moudeden, Y., & Forbes, J. M. (2014). Quasi-two-day wave structure, interannual
 451 variability, and tidal interactions during the 2002–2011 decade. *J. Geophys.*
 452 *Res.*, *119*(5), 2241–2260. doi: 10.1002/2013JD020563
- 453 Müller, H. G. (1972). A discussion on D and E region winds over Europe-
 454 Long-period meteor wind oscillations. *Philos. Trans. R. Soc. London.*
 455 *Ser. A, Math. Phys. Sci.*, *271*(1217), 585–599. Retrieved from [https://](https://royalsocietypublishing.org/doi/abs/10.1098/rsta.1972.0026)
 456 royalsocietypublishing.org/doi/abs/10.1098/rsta.1972.0026 doi:
 457 10.1098/rsta.1972.0026
- 458 Nguyen, V. A., Palo, S. E., Lieberman, R. S., Forbes, J. M., Ortland, D. A., &
 459 Siskind, D. E. (2016). Generation of secondary waves arising from non-

- 460 linear interaction between the quasi 2 day wave and the migrating diurnal
 461 tide. *J. Geophys. Res. Atmos.*, *121*(13), 7762–7780. Retrieved from [http://](http://doi.wiley.com/10.1002/2016JD024794)
 462 doi.wiley.com/10.1002/2016JD024794 doi: 10.1002/2016JD024794
- 463 Oberheide, J., Forbes, J. M., Häusler, K., Wu, Q., & Bruinsma, S. L. (2009).
 464 Tropospheric tides from 80 to 400 km: Propagation, interannual variabil-
 465 ity, and solar cycle effects. *J. Geophys. Res. Atmos.*, *114*(23), 1–18. doi:
 466 10.1029/2009JD012388
- 467 Palo, S. E., & Avery, S. K. (1996). Observations of the quasi-two-day wave
 468 in the middle and lower atmosphere over Christmas Island. *J. Geo-*
 469 *phys. Res. Atmos.*, *101*(D8), 12833–12846. Retrieved from [https://](https://agupubs.onlinelibrary.wiley.com/doi/abs/10.1029/96JD00699)
 470 agupubs.onlinelibrary.wiley.com/doi/abs/10.1029/96JD00699 doi:
 471 <https://doi.org/10.1029/96JD00699>
- 472 Palo, S. E., Roble, R. G., & Hagan, M. E. (1999). Middle atmosphere effects of
 473 the quasi-two-day wave determined from a General Circulation Model. *Earth,*
 474 *Planets Sp.*, *51*(7-8), 629–647. Retrieved from [https://doi.org/10.1186/](https://doi.org/10.1186/BF03353221)
 475 [BF03353221](https://doi.org/10.1186/BF03353221) doi: 10.1186/BF03353221
- 476 Pancheva, D. (1988). Travelling quasi-two-day fluctuations in the summer F-region.
 477 *C. R. Acad. Bulg. Sci.*, *41*(11), 41–44.
- 478 Pancheva, D., & Lysenko, I. (1988). Quasi-2-day fluctuations observed in the sum-
 479 mer F region electron maximum. *Bulg. Geophys. J.*, *14*(2), 41–51.
- 480 Pancheva, D., Mukhtarov, P., & Siskind, D. E. (2018). Climatology of the quasi-
 481 2-day waves observed in the MLS/Aura measurements (2005–2014). *J. Atmos.*
 482 *Solar-Terrestrial Phys.*, *171*(April 2017), 210–224. Retrieved from [https://](https://doi.org/10.1016/j.jastp.2017.05.002)
 483 doi.org/10.1016/j.jastp.2017.05.002 doi: 10.1016/j.jastp.2017.05.002
- 484 Pancheva, D., Mukhtarov, P., Siskind, D. E., & Smith, A. K. (2016). Global dis-
 485 tribution and variability of quasi 2 day waves based on the NOGAPS-ALPHA
 486 reanalysis model. *J. Geophys. Res. Sp. Phys.*, *121*(11), 11,422–11,449. doi:
 487 10.1002/2016JA023381
- 488 Pfister, L. (1985). Baroclinic instability of easterly jets with applications to the sum-
 489 mer mesosphere. *J. Atmos. Sci.*, *42*(4), 313–330. doi: 10.1175/1520-0469(1985)
 490 042<0313:BIOEJW>2.0.CO;2
- 491 Plumb, R. A. (1983). Baroclinic instability of the summer mesosphere: a mechanism
 492 for the quasi-two-day wave? *J. Atmos. Sci.*, *40*(1), 262–270. doi: 10.1175/1520

- 493 -0469(1983)040(0262:BIOTSM)2.0.CO;2
- 494 Randel, W. J. (1994). Observations of the 2-day wave in NMC stratospheric anal-
 495 yses. *J. Atmos. Sci.*, *51*(2), 306–313. doi: 10.1175/1520-0469(1994)051<0306:
 496 OOTDWI>2.0.CO;2
- 497 Rao, N. V., Ratnam, M. V., Vedavathi, C., Tsuda, T., Murthy, B. V. K., Sathishku-
 498 mar, S., . . . Rao, S. V. B. (2017). Seasonal, inter-annual and solar cycle
 499 variability of the quasi two day wave in the low-latitude mesosphere and
 500 lower thermosphere. *J. Atmos. Solar-Terrestrial Phys.*, *152-153*, 20–29.
 501 Retrieved from [https://www.sciencedirect.com/science/article/pii/
 502 S1364682616304084](https://www.sciencedirect.com/science/article/pii/S1364682616304084) doi: <https://doi.org/10.1016/j.jastp.2016.11.005>
- 503 Rao, S. V. B., Eswaraiah, S., Venkat Ratnam, M., Kosalendra, E., Kishore Kumar,
 504 K., Sathish Kumar, S., . . . Gurubaran, S. (2014). Advanced meteor radar
 505 installed at Tirupati: System details and comparison with different radars. *J.*
 506 *Geophys. Res.*, *119*(21), 11,893–11,904. doi: 10.1002/2014JD021781
- 507 Salby, M. L. (1981). Rossby normal modes in nonuniform background configurations.
 508 Part II: Equinox and solstice conditions. *J. Atmos. Sci.*, *38*(9), 1827–1840. doi:
 509 10.1175/1520-0469(1981)038<1827:RNMINB>2.0.CO;2
- 510 Salby, M. L., & Roper, R. G. (1980). Long-Period Oscillations in the Meteor Region.
 511 *J. Atmos. Sci.*, *37*(1), 237–244. doi: 10.1175/1520-0469(1980)037<0237:lpoitm>
 512 2.0.co;2
- 513 Teitelbaum, H., & Vial, F. (1991). On tidal variability induced by nonlinear interac-
 514 tion with planetary waves. *J. Geophys. Res. Sp. Phys.*, *96*(A8), 14169–14178.
 515 Retrieved from <http://doi.wiley.com/10.1029/91JA01019> doi: 10.1029/
 516 91ja01019
- 517 Tunbridge, V. M., Sandford, D. J., & Mitchell, N. J. (2011). Zonal wave numbers
 518 of the summertime 2 day planetary wave observed in the mesosphere by EOS
 519 Aura Microwave Limb Sounder. *J. Geophys. Res. Atmos.*, *116*(11), 1–16. doi:
 520 10.1029/2010JD014567
- 521 Wang, Y., Li, G., Ning, B., Yang, S., Sun, W., & Yu, Y. (2019). All-Sky Inter-
 522 ferometric Meteor Radar Observations of Zonal Structure and Drifts of Low-
 523 Latitude Ionospheric E Region Irregularities. *Earth Sp. Sci.*, *6*(12), 2653–2662.
 524 doi: 10.1029/2019EA000884
- 525 Ward, W. E., Wang, D. Y., Solheim, B. H., & Shepherd, G. G. (1996). Observations

- 526 of the two-day wave in WINDII data during January, 1993. *Geophys. Res.*
527 *Lett.*, *23*(21), 2923–2926. doi: 10.1029/96GL02897
- 528 Wu, D. L., Hays, P. B., Skinner, W. R., Marshall, A. R., Burrage, M. D., Lieber-
529 man, R. S., & Ortland, D. A. (1993). Observations of the quasi 2-day wave
530 from the High Resolution Doppler Imager on Uars. *Geophys. Res. Lett.*,
531 *20*(24), 2853–2856. Retrieved from <https://doi.org/10.1029/93gl03008>
532 doi: 10.1029/93GL03008
- 533 Yue, J., Liu, H. L., & Chang, L. C. (2012, mar). Numerical investigation of the
534 quasi 2 day wave in the mesosphere and lower thermosphere. *J. Geophys. Res.*
535 *Atmos.*, *117*(5). doi: 10.1029/2011JD016574
- 536 Yue, J., Wang, W., Richmond, A. D., & Liu, H. L. (2012). Quasi-two-day wave
537 coupling of the mesosphere and lower thermosphere-ionosphere in the TIME-
538 GCM: Two-day oscillations in the ionosphere. *J. Geophys. Res. Sp. Phys.*,
539 *117*(7). doi: 10.1029/2012JA017815
- 540 Yue, J., Wang, W., Ruan, H., Chang, L. C., & Lei, J. (2016). Impact of the in-
541 teraction between the quasi-2 day wave and tides on the ionosphere and
542 thermosphere. *J. Geophys. Res. A Sp. Phys.*, *121*(4), 3555–3563. doi:
543 10.1002/2016JA022444

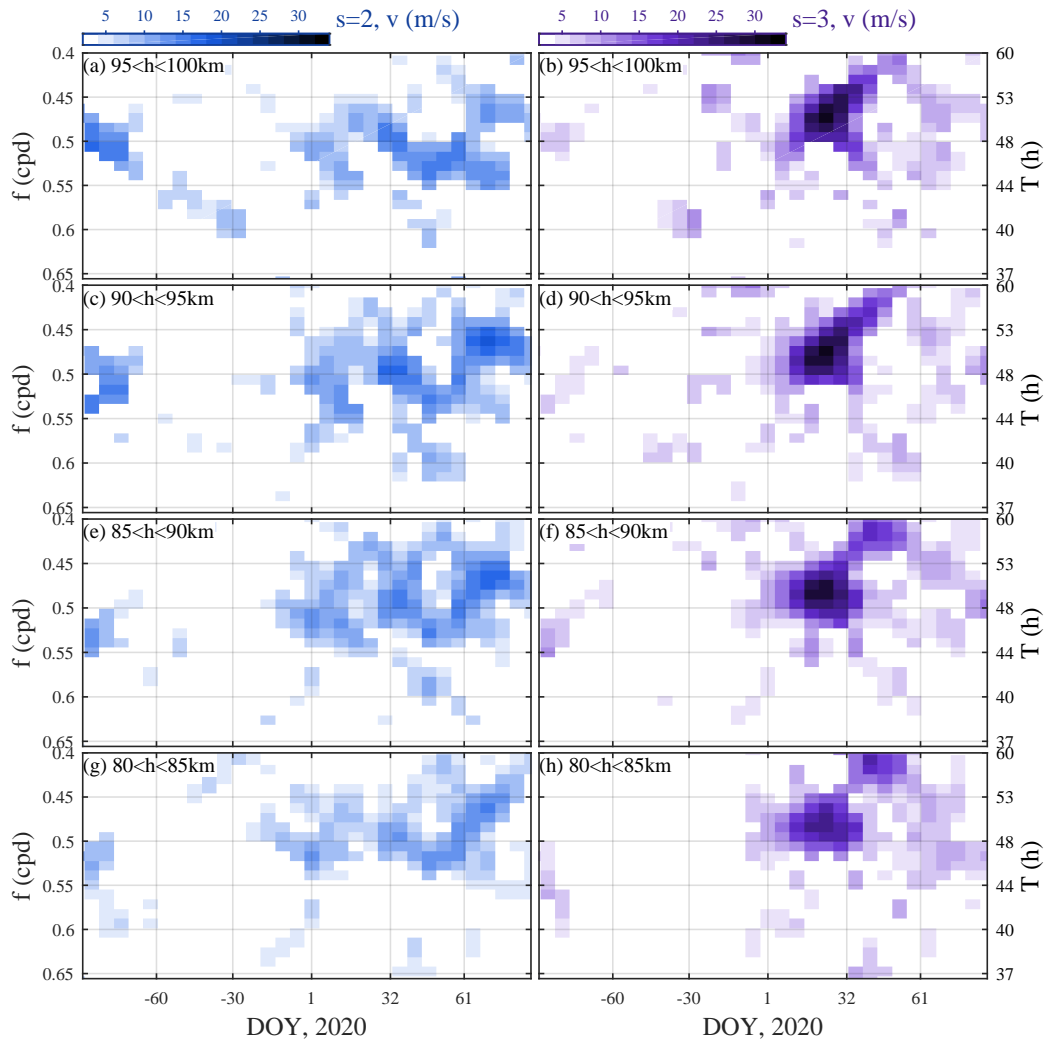


Figure 1: Amplitudes of (blue) Q2DW+2 and (purple) Q2DW+3 in time-frequency depiction, in four altitude ranges estimated using the meridional winds from the four low-latitude radars.

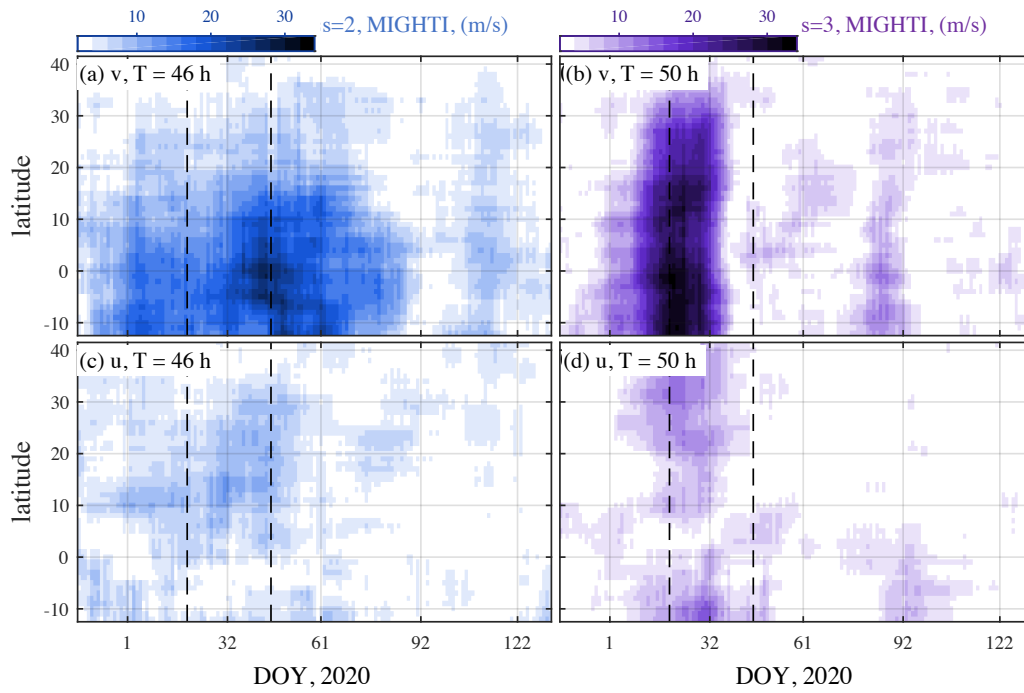


Figure 2: (a) Q2DW+2 amplitude at 46 h period at 98 km altitude in time-latitude depiction estimated from MIGHTI meridional wind. (b) same as (a) but for Q2DW+3 at 50 h period. (c,d) same as (a,b) but estimated from zonal winds. Vertical dashed lines indicate the centers of two 9-day windows used in Figure 4, which contain the maxima of the amplitudes and where daytime wind data are available above 106 km.

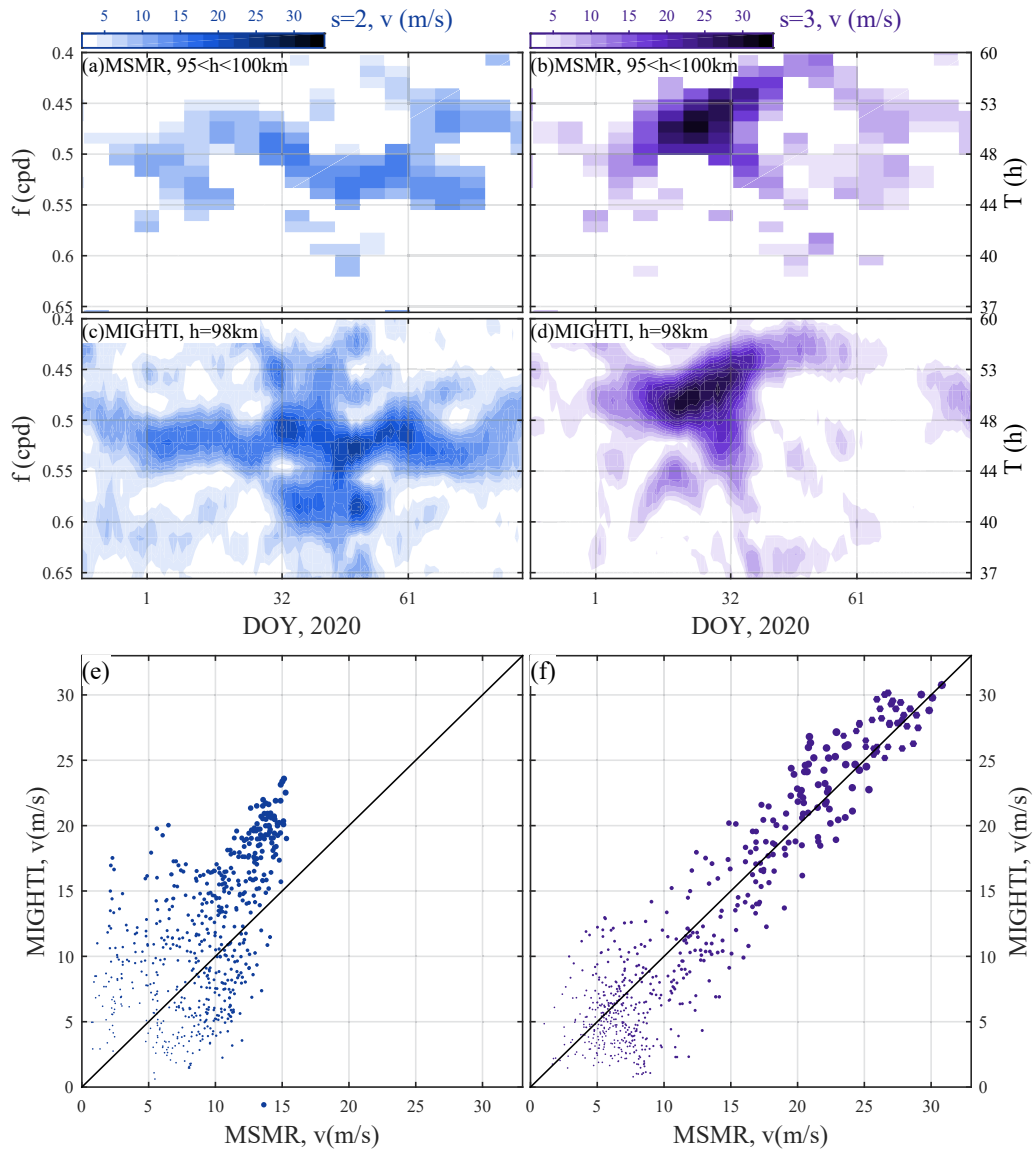


Figure 3: Meridional wind Q2DW+2 and Q2DW+3 amplitude comparisons between MSMR and MIGHTI results. (a, b) MSMR results between 95–100 km for $s = 2$ and $s = 3$, and (c, d) same plots as (a, b) but estimated from MIGHTI winds at 98 km altitude. (e) scatter plot of the values sampled from (a) and (c), in which each point denotes one pixel in (c) and its size is weighted by the sum of the amplitudes' squared. (f) same plots as (e) but sampled from (b) and (d).

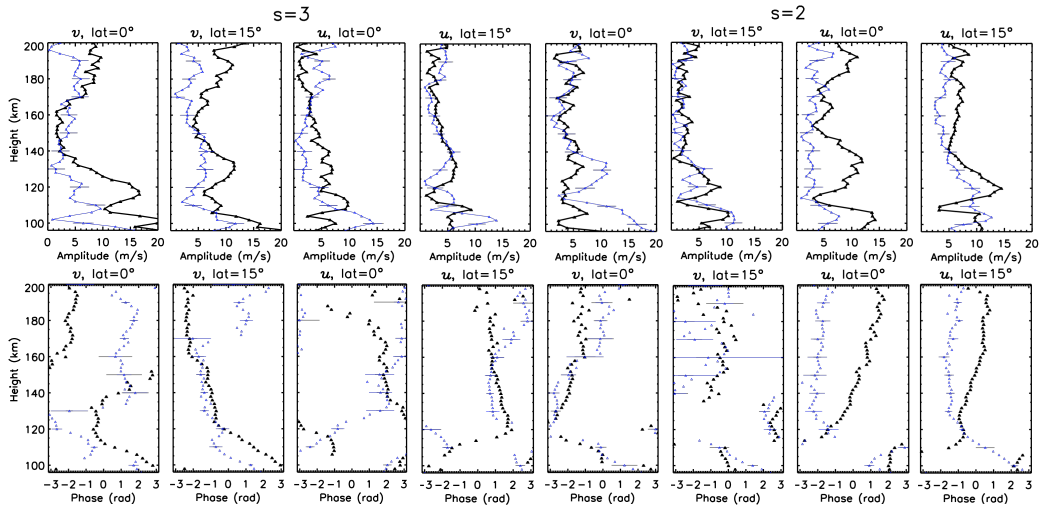


Figure 4: Vertical profiles of amplitude (top) and phase (bottom) u and v centered on latitudes 0° and 15° for Q2DW+3 (left four columns) and Q2DW+2 (right four columns) for DOY 15–23 (black) and DOY 41–49 (blue).